From Short Circuit to Completed Circuit

Conductive Hydrogel Facilitating Oral Wound Healing

Zhou, Qiangqiang; Dai, Hanqing; Yan, Yukun; Qin, Zhiming; Zhou, Mengqi; Zhang, Wanlu; Zhang, Guoqi; Guo, Ruiqian; Wei, Xiaoling

DOI
10.1002/adhm.202303143

Publication date
2024

Document Version
Final published version

Published in
Advanced Healthcare Materials

Citation (APA)
Zhou, Q., Dai, H., Yan, Y., Qin, Z., Zhou, M., Zhang, W., Zhang, G., Guo, R., & Wei, X. (2024). From Short Circuit to Completed Circuit: Conductive Hydrogel Facilitating Oral Wound Healing. *Advanced Healthcare Materials*, *13*(15), Article 2303143. https://doi.org/10.1002/adhm.202303143

ADVANCED HEALTHCARE MATERIALS
www.advhealthmat.de

From Short Circuit to Completed Circuit: Conductive Hydrogel Facilitating Oral Wound Healing

Qiangqiang Zhou, Hanqing Dai, Yukun Yan, Zhiming Qin, Mengqi Zhou, Wanlu Zhang, Guoqi Zhang, Ruiqian Guo,* and Xiaoling Wei**

The primary challenges posed by oral mucosal diseases are their high incidence and the difficulty in managing symptoms. Inspired by the ability of bioelectricity to activate cells, accelerate metabolism, and enhance immunity, a conductive polyacrylamide/sodium alginate crosslinked hydrogel composite containing reduced graphene oxide (PAA-SA@rGO) is developed. This composite possesses antibacterial, anti-inflammatory, and antioxidant properties, serving as a bridge to turn the "short circuit" of the injured site into a "completed circuit," thereby prompting fibroblasts in proximity to the wound site to secrete growth factors and expedite tissue regeneration. Simultaneously, the PAA-SA@rGO hydrogel effectively seals wounds to form a barrier, exhibits antibacterial and anti-inflammatory properties, and prevents foreign bacterial invasion. As the electric field of the wound is rebuilt and repaired by the PAA-SA@rGO hydrogel, a 5 × 5 mm^2 wound in the full-thickness buccal mucosa of rats can be expeditiously mended within mere 7 days. The theoretical calculations indicate that the PAA-SA@rGO hydrogel can aggregate and express SOX2, PITX1, and PITX2 at the wound site, which has a promoting effect on rapid wound healing. Importantly, this PAA-SA@rGO hydrogel has a fast curative effect and only needs to be applied for the first three days, which significantly improves patient satisfaction during treatment.

1. Introduction

Oral mucosal defects are a series of conditions caused by the shedding of necrotic tissue, impacting both the oral mucosa and soft tissue, significantly compromising patients' quality of life.[1] However, the human oral flora is complex, and its changes are affected by various factors, including exogenous food intake, physical diseases, and drug treatments.[2] Generally, oral wound healing requires sustained hemostasis, inflammation, proliferation, and structural remodeling of damaged tissues, involving a variety of cell types and biological processes.[3–5] Therefore, dressings that can quickly control bleeding and possess antibacterial, anti-inflammatory, and prohealing properties are essential for wound healing and granulation tissue formation.[6] In addition, the inflammatory response affects the structural regeneration of tissues and is regulated by a variety of cytokines and growth factors.[7–9] In the process of wound healing, moderating the escalation of pro-inflammatory cytokines and promoting the proliferation of endothelial cells contribute to alleviate pathologic pain and accelerate repair.[10–13]

Generally, endogenous distributions of bioelectricity, primarily governed by ion channels and gap junctions, are ubiquitously present in all tissues, actively participating in various physiological activities.[14,15] When the body is stimulated externally, electrical signals are activated in preference to chemical signals and are transmitted between cells and tissues.[16] Specifically, the generation of action potential involves the movement of sodium, potassium, and chloride ions across the cell membrane, subsequently

Q. Zhou, Z. Qin, M. Zhou, X. Wei
Department of Operative Dentistry and Endodontics
Shanghai Stomatological Hospital and School of Stomatology
Fudan University
Shanghai 200001, China
E-mail: xiaoling_wei@fudan.edu.cn
Q. Zhou, Z. Qin, M. Zhou, X. Wei
Shanghai Key Laboratory of Craniomaxillofacial Development and Diseases
Fudan University
Shanghai 200001, China

H. Dai, R. Guo
Academy for Engineering and Technology
Fudan University
Shanghai 200433, China
E-mail: daihq@fudan.edu.cn; rqguo@fudan.edu.cn
Y. Yan, W. Zhang, R. Guo
Institute for Electric Light Sources
Fudan University
Shanghai 200433, China
G. Zhang
Electronic Components Technology and Materials
Delft University of Technology
Delft 2628 CD, The Netherlands

The ORCID identification number(s) for the author(s) of this article can be found under https://doi.org/10.1002/adhm.202303143

DOI: 10.1002/adhm.202303143

triggering a cascade of events that elicit genetic-level responses within the cell.[17,18] Numerous studies have demonstrated that diverse endogenous bioelectrical signals play crucial roles in regulating life processes, and stable bioelectrical states are essential for cellular gene expression, intercellular communication, and organ development.[18–22] However, localized injuries may disrupt the bioelectrical pathway, leading to a "short circuit", resulting in a deviation of the electric field at the site from that of the surrounding area.[18,20,21] This alteration in the electric field has the potential to disrupt the entire electrophysiological microenvironment, thereby impeding the migration of reparative cells towards the wound.[22] Recent research has underscored the efficacy of electrical stimulation therapy in enhancing tissue perfusion and facilitate cellular proliferation and migration, thereby expediting wound healing through the interaction between externally applied electric fields and endogenous bioelectric phenomena.[23–28] However, the response of specific cells and the underlying mechanisms governing the attainment of biological effects and the acceleration of tissue repair through the regulation of endogenous electric fields remains elusive. This has impeded the achievement of desired outcomes through the simple application of external electrical stimulation. Therefore, the development of electrical biomaterials that are able to effectively couple with endogenous biological electric fields, facilitate the interaction between electrical and chemical signals at the cellular and tissue levels, and enable efficient ion flow between cells holds significant value.

Currently, hydrogel-based flexible power sources and nanogenerators are widely utilized in skin wound healing due to their ability to maintain a moist environment, isolate external air, and exhibit excellent biocompatibility.[29–32] Owing to the constantly humid and dark microbiome environment of the oral cavity, wound repair in this area differs from that of the skin surface.[33,34] Additionally, the presence of oral secretions, irregular wound shapes, and exudates can impede the efficacy of metal electrodes on wounds.[35,36] Therefore, electrical stimulation treatments that are effective for skin wounds may not be suitable for addressing oral wounds.

To address these challenges, we have developed an antibacterial, anti-inflammatory and conductive PAA-SA@rGO hydrogel. In the intraoral environment, the PAA-SA@rGO hydrogel is able to seal the wound, turning the "short circuit" of the injured site into a "completed circuit," and allow the electric field of the wound to be rebuilt and repaired. These electric field changes have the capacity to direct the repair cells to move towards the wound, facilitating the rapid repair of the damaged area. Additionally, the PAA-SA@rGO hydrogel can form a protective barrier on the wound, playing an antibacterial and anti-inflammatory role, and prevent foreign bacteria from invading. The results show that the full-layer buccal mucosa of rats with 5 × 5 mm^2 wounds could be quickly repaired within 7 days. The theoretical calculations indicate that the PAA-SA@rGO hydrogel had the ability to aggregate and express SOX2, PITX1, and PITX2 at the wound site, which had a promoting effect on rapid wound healing. Notably, this PAA-SA@rGO hydrogel boasts not only rapid efficacy, but also the convenience of noncontinuous wound attachment, and only needs to be applied in the first three days of a treatment, which will significantly improving patient comfort during the healing process. Hence, this work has the capacity to provide a new design template, optimization idea and development direction for bioelectric construction and bioactive electronic stimulation of wound healing.

2. Results and Discussion

The oral cavity is a naturally moist and complex environment with many bacteria. Acute trauma to the loose mucous tissue often results in bleeding, infection, and pain. The frictional movement of oral mucosa such as chewing, speaking and swallowing often leads to delayed wound healing. To address these challenges, we propose to construct a bioelectric "completed circuit" therapy for oral wounds. In detail, normal oral tissue forms a completion pathway bioelectrical network, and when oral tissue is damaged, the bioelectrical network at that location is also damaged, forming a "short circuit" (**Figure 1a**). Therefore, we designed a PAA-SA@rGO hydrogel with high biosafety and good biocompatibility by the free radical polymerization (detailed in the Experimental Section). One of the key components in the PAA-SA dual network hydrogel scaffolds is rGO, which plays a significant role. Firstly, rGO acts as a nano-reinforcement material, enhancing the mechanical and adhesive properties of the scaffolds, while also reducing swelling. Secondly, the uniformly distributed rGO within the scaffolds forms an excellent electronic pathway, facilitating the transmission of electrical signals.[37,38] Furthermore, the addition of graphene provides the hydrogels with advantageous oxygen radical scavenging and antioxidant properties.[39,40] This hydrogel acts as a bridge of bioelectric field, sealing the wound and turning the "short circuit" at the injured site into a "completed circuit" (Figure 1a). After reconstruction and repair, the changes in the electric field at the wound site have the capacity to guide repair cells toward the wound, facilitating the rapid repair of the damaged tissue. The morphology of the PAA-SA and PAA-SA@rGO hydrogel had been fully investigated (Figure 1b,c), and the wavy appearance of the PAA-SA@rGO hydrogel is similar to that of the sea wave. The tensile test results displayed that this PAA-SA@rGO hydrogel had excellent flexibility and could be stretched to 3 times its original length (Figure 1e,f). The oral cavity is a complex environment, and hydrogel dressings must maintain strong adhesion under humid and dynamic conditions (Movie S1, Supporting Information). Therefore, we further characterized the adhesion and swelling properties of hydrogels. The results showed that PAA-SA@rGO had lower swelling ability compared to PAA-SA hydrogel (Figure S1, Supporting Information). Due to this slower swelling rate, the hydrogel was restricted to swell and stretch after absorbing excess water in a moist oral environment. Additionally, we tested the adhesion properties of the PAA-SA and PAA-SA@rGO under dry and wet conditions (Figure 1d and Figure S2, Supporting Information). Although moisture did have some effect on the adhesion properties, PAA-SA@rGO was still able to withstand a tensile force of ≈1 N on wet tissue surfaces (Figure S2, Supporting Information). Furthermore, through consecutive photographs taken at 6-hour intervals (Figure S3, Supporting Information), we observed that the PAA-SA@rGO hydrogel maintained its integrity for over 24 hours during regular feeding activities in actual buccal mucosal wounds of Sprague-Dawley (SD) rats. The adhesion mechanism of PAA-SA@rGO hydrogel is likely attributed to the synergistic effect of multiple factors. According to the previous

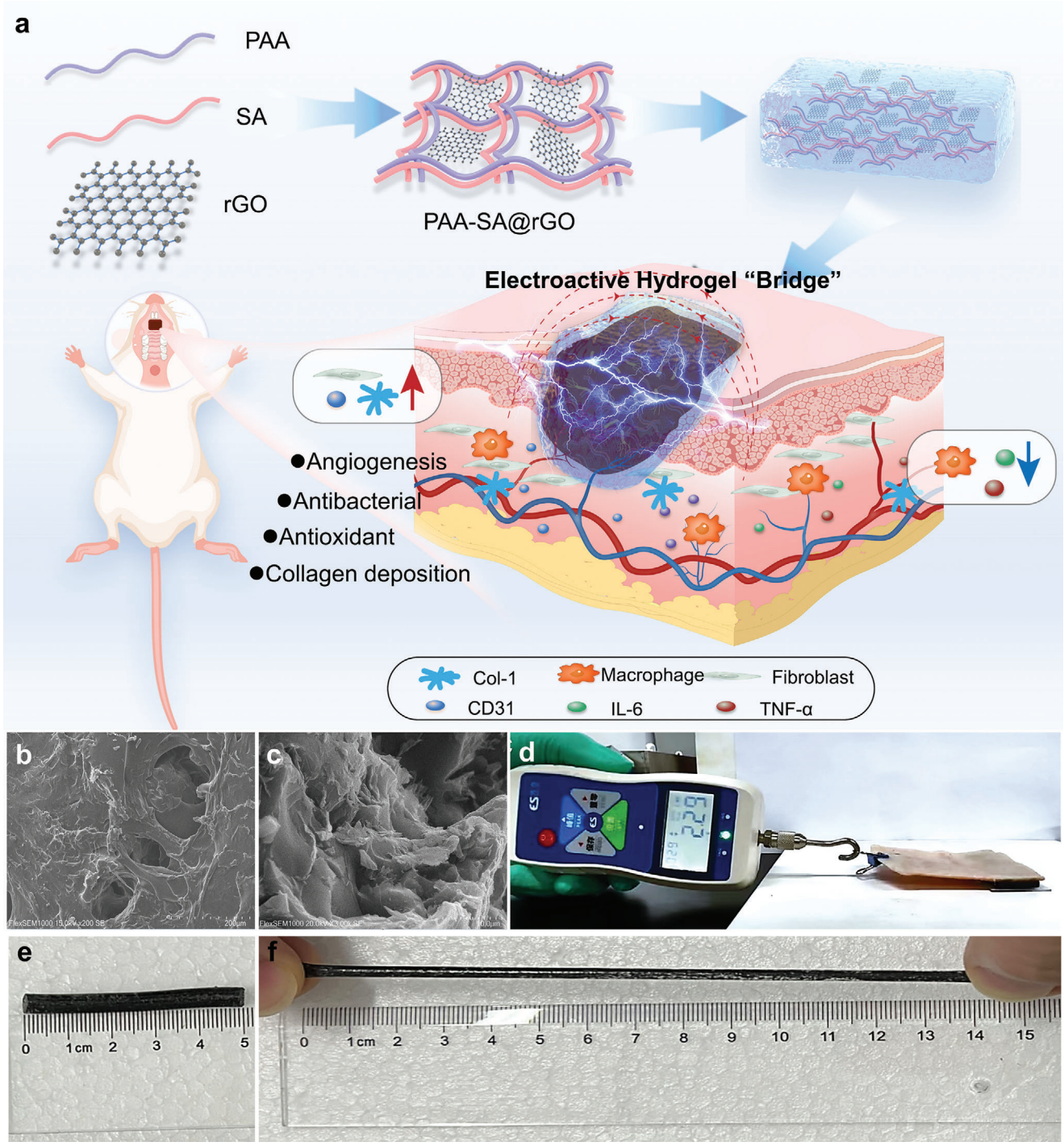

Figure 1. Electric field reconstruction strategy and the properties of the PAA-SA@rGO hydrogel. a) The PAA-SA@rGO hydrogel bridge creates a bioelectric "completed circuit" therapy for oral wounds, rectifying the "short circuit" state at the injury site. This reconstruction of the electric field microenvironment accelerates the healing of oral mucosal wounds. SEM image of the PAA-SA b) and the PAA-SA@rGO c) hydrogel. d) Adhesion of the PAA-SA@rGO hydrogel under dry conditions. e,f) Flexibility testing the PAA-SA@rGO hydrogel.

reports,[41–43] sodium alginate contains a large number of carboxyl groups in its structure, and its bioadhesion is related to the hydrogen bond between hydrophilic functional group (–COOH) and mucoglycoprotein. Moreover, there are many rGO and negative/cationic groups on the surface of hydrogels that participate in a variety of noncovalent bonding, including hydrogen bonding and cation-π interaction, which contribute to the adhesion properties of PAA-SA@rGO. These factors collectively contribute to the PAA-SA@rGO hydrogel achieving effective adhesion in the dynamic and moist oral environment.

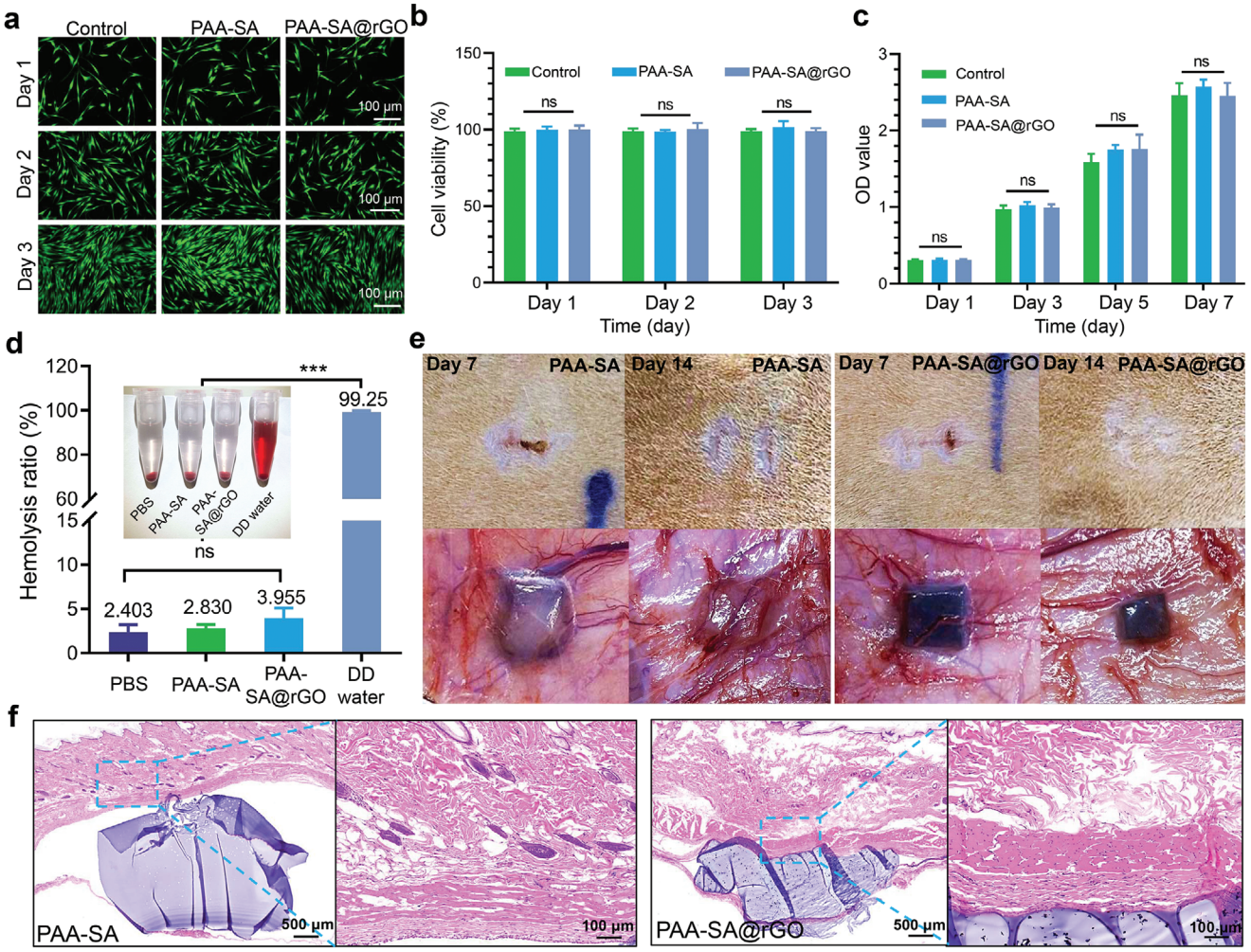

Figure 2. Biocompatibility and biosafety of the hydrogels in vitro *and* in vivo. a) Live/dead staining of fibroblasts after incubation in hydrogel extracts for 1, 2, and 3 days. Scale bar: 100 μm. b) Cell viability of fibroblasts after incubation in hydrogel extracts for 1, 2, and 3 days at 37 °C. c) The CCK-8 results of fibroblasts cultured with the samples prepared using the control and hydrogels for 7 days. d) Evaluation of the hemolysis properties of hydrogels in vitro and quantification of the PAA-SA and PAA-SA@rGO hemolysis ratios. e) Photographs of surgical wounds after 7 and 14 days. The degradation of the material was observed after the incision. f) Hematoxylin–eosin staining results of surrounding tissues implanted with the hydrogels in rats on day 14. (*P< 0.05, **P< 0.01, ***P< 0.001, ns: no statistical differences).

Fibroblasts participate in the whole process of tissue healing, and their migration and function change affect the healing effect. To assess the influence of PAA-SA and PAA-SA@rGO hydrogels on modulating the behavior of buccal mucosal fibroblasts, tests were performed to validate the biosafety and proliferation of the PAA-SA and PAA-SA@rGO hydrogels both in vitro and in animal models. As shown in **Figure 2**a, cell numbers increased overtime in all groups, live/dead cell staining (Figure 2a) and quantitative analysis (Figure 2b) of the blank, PAA-SA, and PAA-SA@rGO groups revealed that the PAA-SA@rGO hydrogel had no cytotoxic effects. The CCK-8 results (Figure 2c) further confirmed the proliferation activity of cells in all groups. After culturing for 1, 3, 5, or 7 days, there was little difference in cell growth among these groups, the difference was not statistically significant. These results demonstrated the excellent biocompatibility of the PAA-SA and PAA-SA@rGO hydrogels.

Furthermore, the hemolysis results indicated that the extracts from the PAA-SA and PAA-SA@rGO groups did not cause erythrocyte rupture after contact with blood cell components, and the centrifuged supernatant appeared colorless and transparent (Figure 2d), which showed no significant difference from the control group within the phosphate-buffered saline (PBS). Moreover, the quantitative results showed that the hemolysis rates of both the PAA-SA (2.83%) and PAA-SA@rGO groups (3.96%) were below the 5% threshold specified by ASTM: F 75-00, which demonstrated excellent blood compatibility of the PAA-SA and PAA-SA@rGO hydrogels. In addition, no death or significant weight loss was observed during the SD rat dorsal subcutaneous implantation experiment. Additionally, there were no evident signs of redness, swelling, ulceration in the wound area, suture detachment, and the wound exhibited satisfactory healing (Figure 2e).

To further assess the inflammatory status of PAA-SA and PAA-SA@rGO hydrogels in the wound, these surrounding

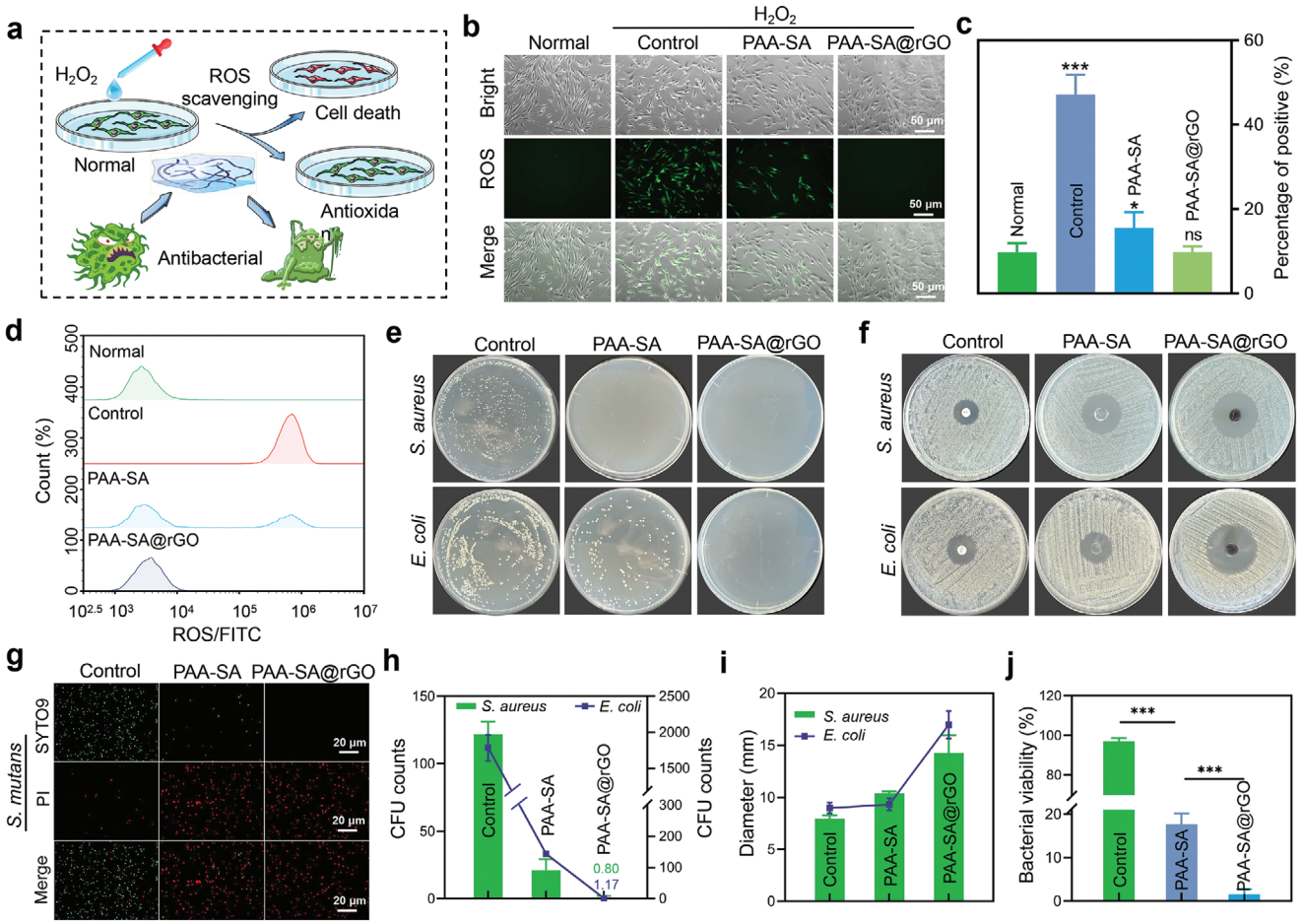

Figure 3. Evaluation of in-vitro antioxidant and antibacterial properties of the PAA-SA and PAA-SA@rGO hydrogel. a) Schematic diagram illustrating the antioxidant and antimicrobial properties of hydrogel systems. b) Representative images of fibroblast cells stained with ROS under different treatment conditions. Scale bar: 50 μm. c) Quantitative analysis of ROS expression in different experimental groups. d) Fluorescence intensity of fibroblasts measured by flow cytometry. Note: In the control group, a new peak emerged, suggesting that a significant number of cells experienced oxidative damage. e) Representative photographs of *S. aureus and E. coli* colony-forming units (CFUs) growth after 18 h. Quantification of colony numbers of *S. aureus* and *E. coli* after incubation (h). f) Photographs of antibacterial zones of *S. aureus* and *E. coli* around the samples, statistical diagram of the antibacterial area (i). g) Representative fluorescent microscopy images of live/dead staining of *S. mutans* after treatment. Scale bar: 20 μm. Calculation of the bacterial survival ratio in each experimental group (j) (*P< 0.05, **P< 0.01, ***P< 0.001, ns: no statistical differences).

tissues implanted with PAA-SA and PAA-SA@rGO hydrogels on day 7 and 14 were stained with hematoxylin and eosin (H&E), respectively. After 7 days of implantation, the results revealed the presence of inflammatory cells and fibrous sacs at the implantation sites of PAA-SA and PAA-SA@rGO hydrogels. Additionally, a limited number of inflammatory cells infiltrated into the interface layer; however, both groups exhibited reduced volume and density compared to preimplantation levels due to the biodegradability of SA hydrogel (Figure S4, Supporting Information). After 14 days of implantation, the inflammation entered a chronic phase, and both PAA-SA and PAA-SA@rGO hydrogels were significantly degraded and absorbed. Inflammatory cell infiltration at the implantation site decreased, and the thickness of the fibrocystic layer also decreased (Figure 2f). These results suggested that both PAA-SA and PAA-SA@rGO hydrogels were safe and biocompatible in vivo. Notably, other studies had confirmed the good biocompatibility of PAA-SA derived hydrogels.[44,45]

Moreover, the antioxidative stress properties of the PAA-SA and PAA-SA@rGO hydrogels were demonstrated by examining the protective effect of hydrogels on fibroblasts under ROS injury (**Figure 3a**). After incubating fibroblasts with H_2O_2 for 2 hours, the cells in the control group exhibited strong green fluorescence compared to the normal group. In contrast, the PAA-SA group displayed a significant reduction in fluorescence intensity (Figure 3b). Approximately 84.51% of ROS were eliminated within 20 minutes in the PAA-SA group (Figure 3c), indicating that the PAA-SA hydrogel possesses scavenging capabilities against ROS in vitro. Additionally, both the PAA-SA and PAA-SA@rGO groups exhibited a significant reduction in intracellular ROS compared to the control group (Figure 3c), with minimal green fluorescence observed in the PAA-SA@rGO hydrogel group (Figure 3b) and a flow distribution peak similar to that of the blank group (Figure 3d). These results suggested that PAA-SA@rGO has a better scavenging effect on ROS and can serve as

an antioxidant for enhanced cellular protection against oxidative stress damage.

Graphene and its derivatives, including rGO, have shown good antibacterial properties.[46] To evaluate the possible antibacterial activity of PAA-SA and PAA-SA@rGO hydrogels, both bacteria counting and live/dead staining were used. Staphylococcus aureus (*S. aureus*) and Escherichia coli (*E. coli*) were used as representatives of gram-positive and Gram-negative bacteria, respectively. And Streptococcus mutans (*S. mutans*) were used as typical representatives of oral pathogens to test the antibacterial ability of the PAA-SA@rGO hydrogel. The results demonstrated a significant reduction in the number of *E. coli* and *S. aureus* colonies on PAA-SA and PAA-SA@rGO hydrogel agar plates (Figure 3e,h). Remarkably, the PAA-SA@rGO hydrogel exhibited a pronounced antibacterial effect on the agar plates, leading to the near-complete eradication of bacteria. The exceptional bactericidal efficacy of the PAA-SA@rGO hydrogel was further validated through live/dead bacterial staining analyses of *S. mutans* (Figure 3g,j). To quantitatively evaluate the antibacterial efficacy of PAA-SA@rGO, we employed the agar diffusion method to measure the size of the antibacterial ring. As depicted in Figure 3f–i, the PAA-SA and PAA-SA@rGO hydrogels demonstrated significant antibacterial activity against *S. aureus* and *E. coli*, with larger antibacterial zones of inhibition observed for the PAA-SA hydrogel (10.40, 9.33) and the PAA-SA@rGO hydrogel (14.25, 17.00) compared to the control group within drug disks (7.95, 8.98) ($P < 0.05$). These results indicated that the PAA-SA@rGO hydrogels exhibited enhanced antibacterial efficacy and were more conducive to oral wound healing.

To verify the therapeutic efficacy of PAA-SA@rGO hydrogel on mucosal wounds in vivo, we established an infected rat buccal mucosal wound model with *S. mutans*, a predominant microorganism in the oral cavity (**Figure 4a**). Subsequently, the wounds were treated with dressings containing basic fibroblast growth factor (bFGF-gel), PAA-SA, and PAA-SA@rGO groups respectively (Figure 4b,c). A control group was also included, where wounds were healed naturally without any intervention. On day 3, the wound healing of each group was significantly improved, with no significant differences observed in the healing areas among all groups (Figure 4b,c). Nevertheless, the wound area of the control group, PAA-SA and bFGF-gel groups exhibited ulcerated surfaces covered with a pseudo-membrane and a central depression (Figure 4b,c). Notably, the PAA-SA@rGO group exhibited notable outcomes, including complete coverage of the wound surface by newly formed granulation tissue, gradual reduction and recovery of the concave surface, as well as decreased redness and swelling around the wound (Figure 4b,c). These effects might be attributed to early adhesion and hemostasis, which facilitated wound contraction, protected the wound surface, and prevented secondary injury caused by chewing.

On day 7, the PAA-SA@rGO hydrogel exhibited accelerated tissue repair, with a significantly reduced wound surface area and a wound healing rate of 92.21%. Its wound healing rate was also significantly higher than that observed in the control group (40.43%), PAA-SA group (66.47%), and commercial bFGF-gel group (73.05%) ($P < 0.05$) (Figure 4d). This might be attributed to the antibacterial effect, which reduces bacterial attack, mitigates inflammatory response, and expedites the inflammatory period. On day 10, the wounds of the control group, PAA-SA group, and commercial growth factor gel group exhibited further reduction. However, residual unhealed wounds along with slight redness and swelling of the mucosa persisted. In contrast, in the PAA-SA@rGO group, complete healing of the mucosa without any scarring was observed, accompanied by visible regeneration of the mucosal frenulum, thereby achieving functional recovery within the wound area. Importantly, the repair effect of the PAA-SA@rGO hydrogel in this work exhibits significant advantages over the findings reported by other researchers in recent years,[3,5,47–52] within the field familiar to the researchers (Figure 4e).

To assess the inflammatory response, tissue healing, and collagen deposition at different time points, we conducted histological analysis using H&E and Masson staining techniques on tissue samples obtained from the wound site (**Figure 5a**). On the 7th day, a remodeled new granulation tissue was observed in the wound area of the PAA-SA@rGO hydrogel group, with a continuous subepithelial muscle layer. The nail bed layer became thinner, and the structural hierarchy remained distinct. (Figure 5a). Although the wounds of the PAA-SA, bFGF-gel, and control groups exhibited new tissue growth towards the wound center, complete healing was not achieved. In the control group, inflammatory cells were still present at the wound margin, and there was incomplete epithelialization. This effectiveness of the PAA-SA@rGO hydrogel in wound healing might be attributed to its ability to create a protective barrier, exhibit antibacterial and anti-inflammatory properties, and prevent the invasion of foreign bacteria. Consequently, it accelerates the progression of wound healing into the proliferation and remodeling stages.

Additionally, the balance between collagen synthesis and degradation plays an important role in wound healing. Masson staining was used to evaluate the situation of new collagen in the wound area (Figure 5b,c). The quantitative analysis showed that the collagen content in the PAA-SA@rGO group (81.58%) was significantly higher than that in the control group (31.06%), PAA-SA hydrogel group (41.01%), and bFGF-gel group (41.01%) ($P < 0.05$). Overall, these results indicated that the PAA-SA@rGO group exhibited potent antibacterial effects, mitigated inflammatory reactions, accelerated tissue regeneration, and facilitated functional reconstruction. Moreover, the wound healing rate in this group was significantly superior to that of the control, PAA-SA and bFGF-gel groups.

To further monitor the situation of new collagen and the inflammatory response during wound healing, we performed immunohistochemical and semi-quantitative analyses of inflammatory factors TNF-α, IL6, CD31, and Col-1 (Figure 5d). As shown in Figure 5e–h, on day 3, the expressions of inflammatory cytokines TNF-α and IL6 in the PAA-SA@rGO hydrogel group were significantly lower than the other three groups. On day 7, the expressions of angiogenic factor CD31 and Col-1 were significantly higher in the PAA-SA@rGO group than the control, PAA-SA, and bFGF-gel groups. This suggested that the PAA-SA@rGO hydrogel could accelerate oral wound closure by reducing inflammation and promoting collagen production.

As a theoretical verification, we simulated the detailed process of electric field reconstruction for the wound site (**Figure 6**). Since the electric field formed by the diffusion of ions in the PAA-SA@rGO hydrogel is the key to its reconstruction of the electric field at the wound, we simulated the diffusion of H^+, OH^-,

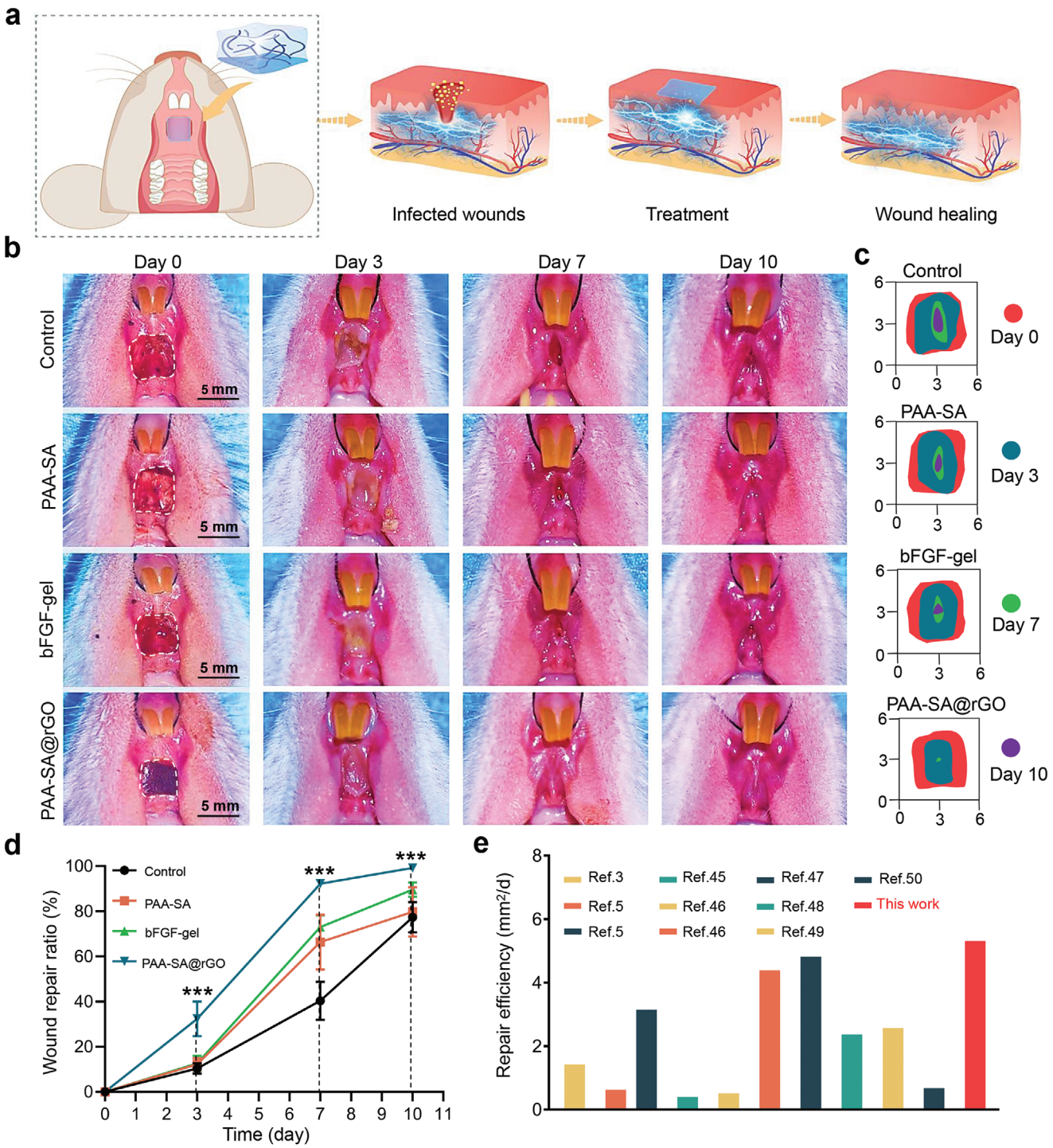

Figure 4. In vivo healing of infected oral mucosal wounds. a) Schematic diagram illustrating the application of PAA-SA@rGO for promoting healing of buccal mucosal defects in a rat model. b) Representative photographs showing the progression of wound healing in the control, PAA-SA, PAA-SA@rGO, and commercially available bFGF-gel groups on day 0, 3, 7, and 10 after wound treatment. c) Schematic representation of wound size after different treatments. d) Quantitative analysis of the remaining wound area and calculation of the wound closure ratio for different dressing groups. e) Comparison of healing efficiency with other studies.[3,5,47–52] (*$P < 0.05$, **$P < 0.01$, ***$P < 0.001$).

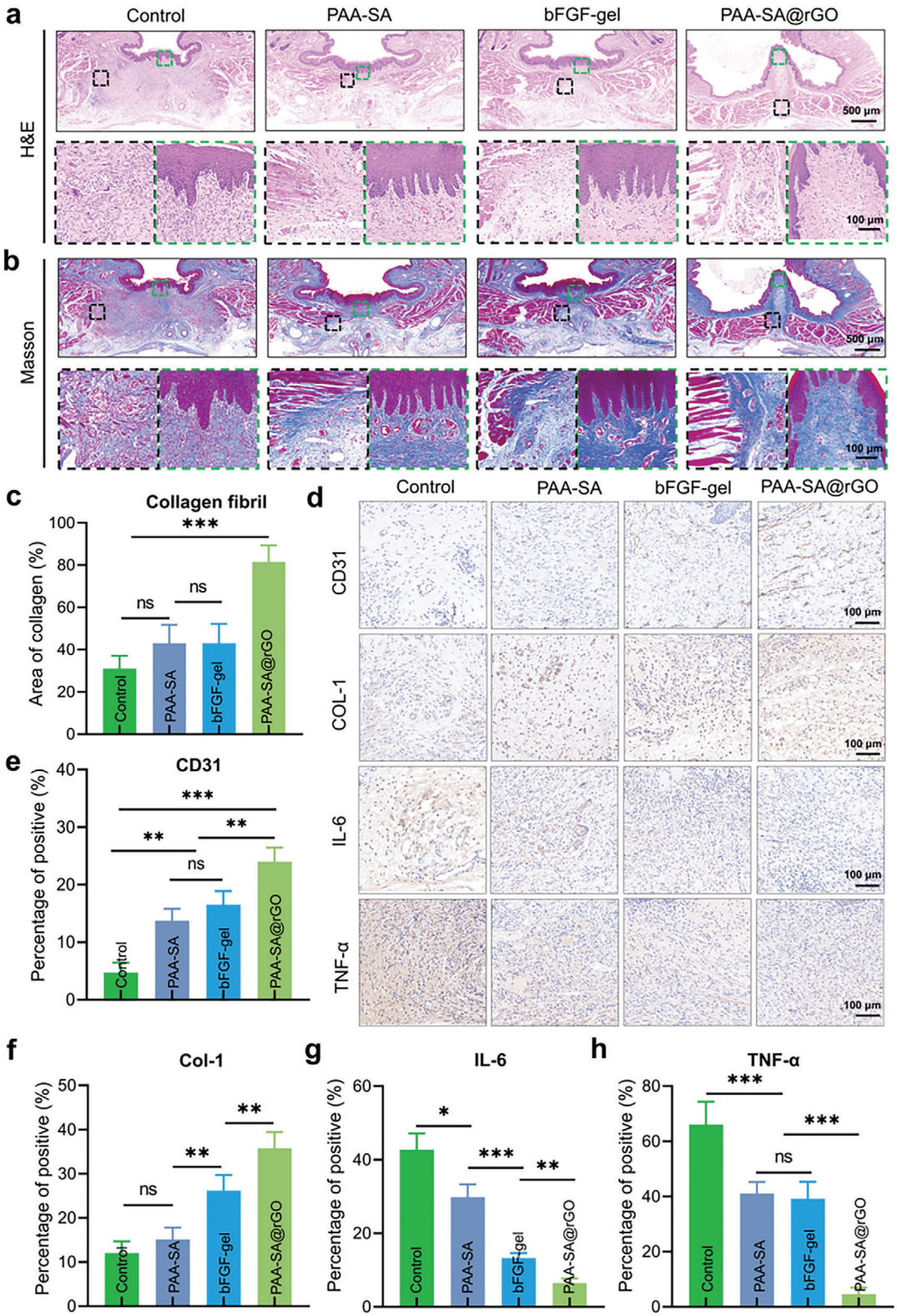

Figure 5. Histological examination of the wound region after 7 days of treatment. a,b) Representative H&E and Masson staining images of oral mucosal wounds in the control, PAA-SA, PAA-SA@rGO, and commercial bFGF-gel dressing groups after treatment. c) Deposited collagen fiber percentages were determined by analyzing the average optical density of different groups. d) Immunofluorescence staining of regenerated mucosal tissue labeled with IL-6, TNF-α, CD31 and Col-1. Scale bars: 100 μm. Quantitative analysis of CD31, Col-1, IL-6 and TNF-α proteins (e–h). (*P< 0.05, **P< 0.01, ***P< 0.001, ns: no statistical differences).

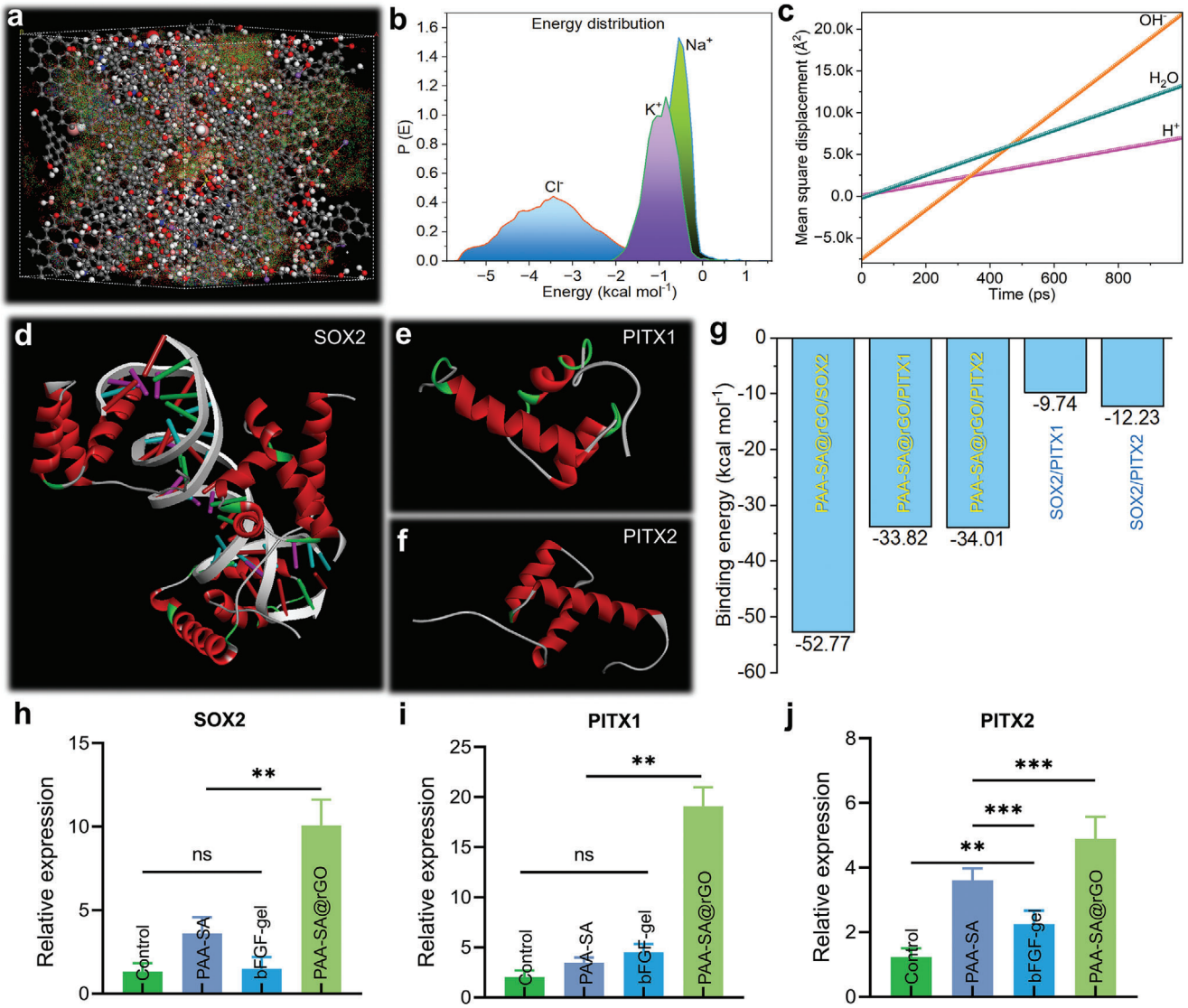

Figure 6. The theoretical calculations of the effect of the PAA-SA@rGO hydrogel on SOX2, PITX1, and PITX2 at the wound site. a) The image of the diffusion of H^+, OH^-, Cl^-, Na^+, and K^+ ions in the wound tissue fluid in the PAA-SA@rGO hydrogel. b) The capacity of Cl^-, Na^+, and K^+ ions. c) The free diffusion coefficients of H^+, OH^- and water molecules in the PAA-SA@rGO hydrogel. The images of d) SOX2, e) PITX1, and f) PITX2. g) Binding energies of PAA-SA@rGO/SOX2, PAA-SA@rGO/PITX1, PAA-SA@rGO/PITX2, SOX2/PITX1 and SOX2/PITX2. Quantification of SOX2, PITX1 and PITX2 mRNA by qRT-PCR in healed tissue samples (h-j).

Cl^-, Na^+, and K^+ ions in the wound tissue fluid in the PAA-SA@rGO hydrogel. Our results indicated that H^+, OH^-, Cl^-, Na^+, and K^+ ions could freely diffuse in the PAA-SA@rGO hydrogel (Figure 6a), and the capacity of Cl^-, Na^+, and K^+ ions was revealed in Figure 6b. Moreover, we observed that the free diffusion coefficients of H^+, OH^- and water molecules in the PAA-SA@rGO hydrogel were 1.15, 4.90, and 2.24 $Å^2$ ps, respectively (Figure 6c), which facilitates the free movement of Cl^-, Na^+, and K^+ ions in the wound tissue fluid in the PAA-SA@rGO hydrogel.

Additionally, the report results suggested that transcriptional regulators, including sex-determining region Y-box 2 (SOX2), paired-like homeodomain 1 (PITX1) and paired-like homeodomain 2 (PITX2) hold the key to the activation of the molecular events responsible for accelerated wound resolution in oral healing.[53] Here, we simulated the interaction among PAA-SA@rGO hydrogel, SOX2 (Figure 6d, here its crystal structure is a POU/HMG/DNA ternary complex), PITX1 (Figure 6e), and PITX2 (Figure 6f), aiming to reveal the effect of PAA-SA@rGO hydrogel on the expression of these regulators at the wound site (Figure 6d–g). The binding energies of PAA-SA@rGO/SOX2, PAA-SA@rGO/PITX1, PAA-SA@rGO/PITX2, SOX2/PITX1, and SOX2/PITX2 were −52.77, −33.82, −34.01, −9.74, and −12.23 kcal mol^{-1} respectively (Figure 6g). These findings indicated that the PAA-SA@rGO hydrogel exhibits a strong adsorption effect on SOX2, PITX1, and PITX2 at the wound site, ultimately promoting rapid wound healing. To assess the potential involvement of transcription factors in facilitating oral wound healing, we conducted a study where whole wound tissues were

treated and subsequently analyzed for the expression of SOX2, PITX1, and PITX2 mRNA. Through quantitative real-time polymerase chain reaction (qRT-PCR) analysis (Figure 6h–j), we observed a significant upregulation of SOX2, PITX1, and PITX2 mRNA levels in rat wound tissues treated with PAA-SA@rGO hydrogel ($P < 0.05$).

Ultimately, we established a buccal mucosa wound model and obtained frozen sections 12 hours after the intervention (**Figure** 7a). The results demonstrated that the PAA-SA@rGO hydrogel enhanced the expression of Nrf2 and HO-1 in the ROS antioxidant signaling pathway (Figure 7b,c). This provides further evidence supporting the role of PAA-SA@rGO hydrogels in protecting wounds from oxidative damage and reducing early inflammatory responses. These findings are consistent with previous reports.[54,55] To verify the impact of the PAA-SA@rGO hydrogel on the electrophysiological microenvironment, we conducted measurements of the wound area's physiological voltage and resistance. The findings revealed that upon application of PAA-SA@rGO hydrogel for wound repair, there was a significant increase in voltage at both ends of the wound compared to the control group ($P < 0.05$) (Figure 7f). The resistance of the wound area treated with PAA-SA@rGO (2.067 MΩ) was significantly lower compared to that of the PAA-SA group (3.423 MΩ) and the untreated wound (5.923 MΩ), while being similar to that of normal tissues (2.027 MΩ) (Figure 7d,e). These findings suggested that the proposed bioelectric "completed circuit" therapy at the oral wound could effectively modify the "short circuit" state of the injured region, reconstruct and restore the electric field microenvironment at the wound site, and guide reparative cells towards prompt restoration of damaged tissue. In essence, the PAA-SA@rGO hydrogel serves as a bridge for systematic electrophysiological regulation, facilitating the full mobilization of electrotactic cells towards the wound site and expediting tissue repair.

3. Conclusions

In summary, we developed a conductive hydrogel composite, consisting of crosslinked polyacrylamide and sodium alginate, incorporated with reduced graphene oxide (PAA-SA@rGO). The results reveal that the composite possesses antibacterial, anti-inflammatory, and antioxidant properties, serving as a bridge to transform the "short circuit" at the injury site into a "completed circuit", thereby stimulating fibroblasts in close proximity to the wound to secrete growth factors and accelerate tissue regeneration. Moreover, the PAA-SA@rGO hydrogel can effectively establish a protective barrier on the wound, exerting potent antibacterial and anti-inflammatory properties to impede the invasion of foreign bacteria. The findings demonstrate that the complete-layer buccal mucosa of rats with 5 × 5 mm^2 wounds can undergo rapid repair within 7 days. Moreover, this PAA-SA@rGO hydrogel not only exhibits swift efficacy but also offers the convenience of noncontinuous wound attachment, requiring application solely during the initial 3 days of treatment. Our study reveals that the PAA-SA@rGO hydrogel induces upregulation of SOX2, PITX1, and PITX2 mRNA through electrophysiological activation cascades. The results, validated by qRT-PCR analysis and theoretical calculations, underscore the hydrogel's role in promoting wound healing by modulating gene expression and ion diffusion in the wound area. This feature significantly enhances patient comfort throughout their healing process. Consequently, this study presents a novel design template, optimization concept, and developmental direction for bioelectric construction and bioactive electronic stimulation in wound healing.

4. Experimental Section

Synthesis of Materials: Raw materials comprise acrylamide (abbreviation "Am"), ammonium persulfate (abbreviation "APS", Aladdin), N, N′-Methylenebisacrylamide (abbreviation "Bis", Aladdin), *N*,*N*,*N*″,*N*′-Tetraethylethylenediamine (abbreviation "TEMED," Aladdin), (3-Acrylamidopropyl) trimethylammonium chloride solution (75 wt% in H_2O, Sigma-Aldrich), sodium isethionate (Aladdin), sodium chloride (Aladdin), phosphate buffer solution (PBS, Servicebio company, Shanghai, China), 10% neutral formalin (Servicebio company, Shanghai, China) and deionized water. Additionally, live/dead bacterial staining assay kit, Hematoxylin-eosin (H&E) and Masson's trichrome Staining Kit were purchased from Beyotime Biological Company (Shanghai, China). Sodium alginate (SA, G:M = 1.5, Mw = 6.4 × 104 g mol^{-1}, viscosity: 200 ± 20 mPa s) was purchased from Sinopharm Chemical ReagentCo., Ltd (Shanghai, China).

The reduced graphene oxide (rGO) was prepared by modified Hummer's method. All hydrogels prepared by free polymerization method are as follows: PAA-SA hydrogel: 2.8 M Am, 0.0065 M Bis, 0.0088 M APS, 0.0094 M TEMED, 0.02 M SA. PAA-SA@rGO hydrogel: 2.8 M Am, 0.0065 M Bis, 0.0088 M APS, 0.0094 M TEMED, 0.02 M SA, rGO 0.02 mg. After mixing the mixtures evenly, a mold containing many holes with 2 cm inner diameter and 0.2 cm depth was used to model the hydrogel by free radical polymerization.

Characterizations of Morphology, Viscosity: The morphology of the samples was obtained by S4800 scanning electron microscopy (SEM) at 5.0 kV. The viscosity and flexibility of hydrogel was characterized by the Suce SH-III digital push-pull meter.

Electrical Signal Characterization: All current-voltage-time relationships are measured by the Keithley 2400 SourceMeter and a Multimeter.

Molecular Dynamics Simulations: The simulation was conducted by Material Studio 2020 software (BIOVIA). The dynamic atomistic simulation was performed according to the following steps:

Step 1: Building Cubic Cells. All simulation cubic boxes (about 25 Å edge) were constructed using amorphous cell module.

Step 2: Molecular Dynamics Simulation. Dynamics simulations were performed at 298K. The cells were subjected to 2 000 000 dynamic steps of 1 fs each at constant mole number, pressure, and temperature (NPT ensemble) to determine their density. This stage was followed by a constant mole number, volume, and temperature (NVT ensemble) refinement stage of 2 000 000 dynamic steps. All molecular dynamics simulations were conducted using Forcite module with COMPASS II force field. The electrostatic term was considered using Ewald and the van der Waals term using atom-based summation methods with an accuracy of 5 × 10^4 kcal mol^{-1}. The repulsive cutoff for Electrostatic term was chosen as 15.5 Å. For NPT molecular dynamics simulations, Nose thermostat and Berendsen barostat were chosen.

Step 3: Analysis. The resulting dynamic trajectories were analyzed using Forcite module analysis tools.

Finally, binding energies and adsorption capacity were performed by Forcite module.

Cytotoxicity Assay In Vitro: Before conducting in vivo experiments, the materials need to undergo in vitro biocompatibility testing. In this study, fibroblast cells were used to evaluate the cytotoxicity of different hydrogel systems. Briefly, the hydrogel materials were thoroughly disinfected prior to the experiment, and a complete culture medium was used to prepare the material extract at a mass ratio of 1 mg mL^{-1}. The fibroblast cells were then cultured with the aforementioned extract, with 4 wells being re-

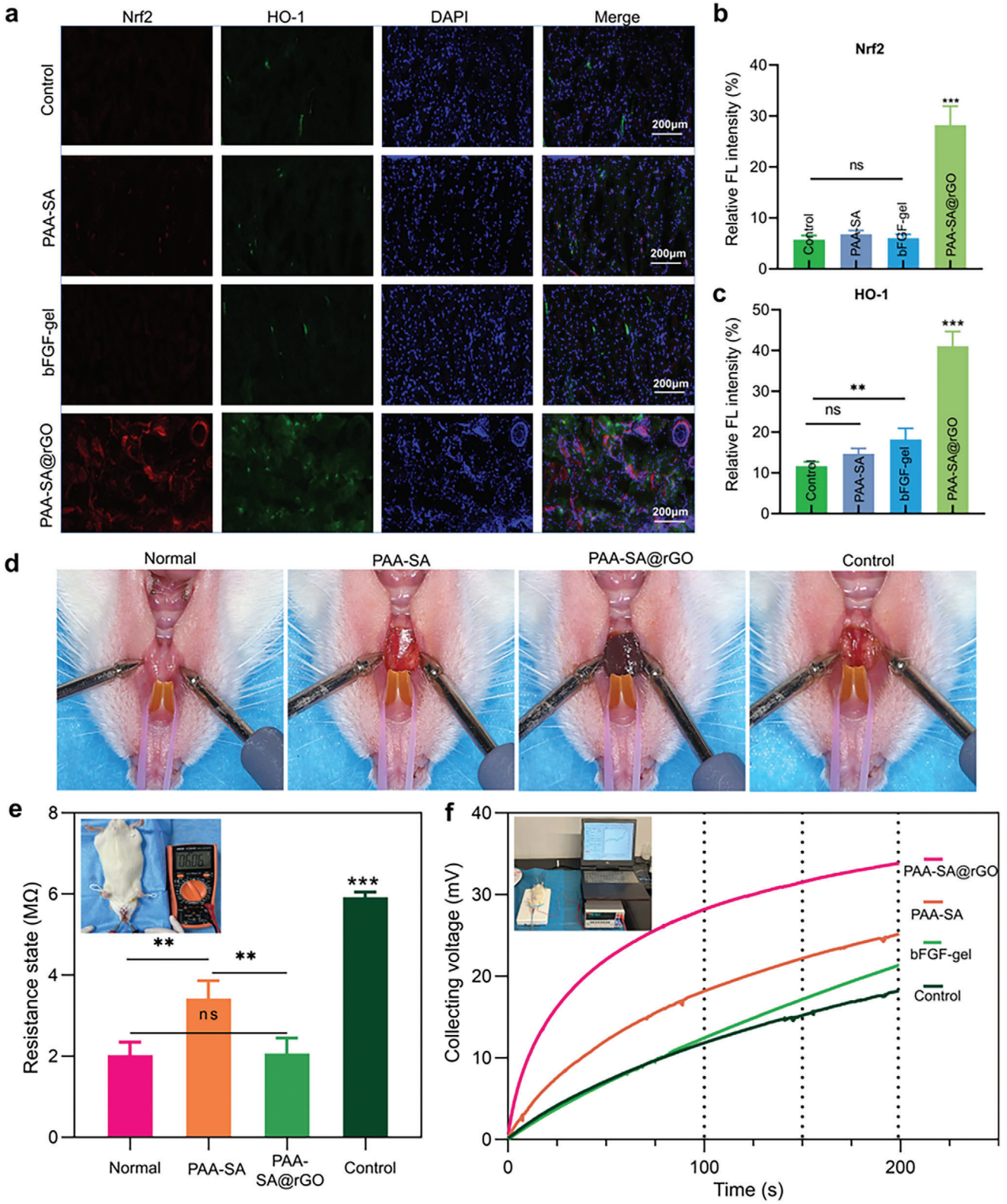

Figure 7. Antioxidant activity and electrical characterization in vivo. b,c) The expression levels of related proteins in (a) were quantitatively analyzed. Scale bar: 200 μm. d) Representative photograph of wound site resistance. e) Quantitative analysis of wound site resistance after different treatments. f) The voltage-time curves at the wound site are presented (*P< 0.05, **P< 0.01, ***P< 0.001, ns: no statistical differences).

peated. A normal culture was set as the control group. The absorbance values (OD) of each well at 450 nm wavelength were measured using a CCK-8 assay kit (Dojindo, Japan) and a microplate photometer (Thermo Scientific) to reflect cell proliferation. Additionally, the Live-Dead Cytotoxicity Assay Kit (Beyotime, China) was used to stain the cells on day 1, day 2, and day 3, and a fluorescence microscope (Leica DMi8, Germany) was used for observation. Live cells were labeled with calcein-AM and emitted green fluorescence, while dead cells were labeled with propidium iodide (PI) and emitted red fluorescence. The cell viability calculation formula is as follows:

$$\text{Cell viability } (\%) = \text{OD (green fluorescence)} / [\text{OD (green fluorescence)} + \text{OD (red fluorescence)}] \times 100\% \quad (1)$$

In Vivo Biosafety Assessment of Hydrogels: The in vivo biocompatibility of the hydrogel material was evaluated using a subcutaneous implantation model in Sprague-Dawley rats. All animal experiments involved in this study were conducted with the approval of the Animal Ethics and Use Committee of the Affiliated Stomatology Hospital of Fudan University. The experimental animals were provided by the Experimental Animal Center of Fudan University. Twelve male SD rats (8–9 weeks old, weighing 200–240 g) were used, with 6 rats in each group. Anesthesia was induced by intraperitoneal injection of 3% pentobarbital sodium (30 mg k^{-1}g). The surgical area was prepared and sterilized, and a 1 cm longitudinal incision was made in the center of the rat's back under sterile conditions. Blunt dissection was performed to create a subcutaneous pocket, and then a hydrogel material measuring $5 \times 5 \times 2$ mm^3 was implanted. The wound was tightly sutured. On postoperative days 7 and 14, the animals were euthanized, and photographs were taken to record wound healing and material degradation. Skin tissue around the material was collected for histological analysis to assess the in vivo safety of the material.

Hemolytic Activity: Hemolysis rate is an important parameter for evaluating the blood compatibility of biomaterials. In this study, the blood compatibility of PAA-SA and PAA-SA@rGO were verified by performing a hemolysis test using SD rat red blood cells. In brief, 5 mL of fresh blood from SD rats was collected using anticoagulant tubes, and a 5% (v/v) red blood cell suspension was prepared by centrifugation, washing, and resuspension. 0.5 mL of the above-mentioned material extract, distilled water (negative control group), 0.9% saline solution (positive control group), and 0.5 mL of red blood cell suspension were mixed and incubated at 37°C for 1 h to observe the hemolysis of red blood cells. 100 µL of the supernatant from each group was taken and added to a 96-well plate, and the absorbance values (OD) was measured at 540 nm using a microplate reader. The hemolysis rate was calculated via the following formula:

$$\text{Hemolysis rate } (\%) = (\text{OD test} - \text{OD negative control}) / (\text{OD positive control} - \text{OD negative control}) \times 100\% \quad (2)$$

Effect of Hydrogels on Antioxidation Damage: When the body is exposed to external stimuli, oxidative stress reactions occur. Reactive oxygen species (ROS) such as hydrogen peroxide, superoxide radicals, and hydroxyl radicals in the body increase. Excessive levels of ROS can cause inflammation and induce cell apoptosis, which is detrimental to wound healing. Therefore, we established an in vitro model of oxidative stress in fibroblasts to investigate the protective effect of the hydrogel system against ROS-induced oxidative damage. In brief, 500×10^{-6} M H_2O_2 was added to fibroblasts in a healthy growth state to induce ROS production. The H_2O_2-induced treatment was set as the control group, and different hydrogel interventions were used as the experimental group. Cells in pure culture medium were used as the normal group. After 2 h of treatment, the culture medium was replaced, and the fluorescence probe DCFH-DA was added according to the instructions of the ROS detection kit for staining. Fluorescence intensity was detected using fluorescence microscopy and flow cytometry (Agilent NovoCyte, USA), and the staining results were quantitatively analyzed using Image J software.

Antibacterial Activities: *S. aureus* (ATCC 6538) and *E. coli* (ATCC 11229) were selected as representative strains of Gram-positive and Gram-negative bacteria, respectively, to evaluate the in vitro antibacterial performance of the hydrogel system. In brief, the hydrogel was cut into circular samples with a diameter of 5 mm and a thickness of 2 mm. These samples were co-cultured with 1 mL bacterial suspension with a concentration of 10^6 CFU mL^{-1} for 12 h. Then, 100 µL of the diluted solution (1000-fold dilution) was inoculated onto agar plates and incubated for an additional 18 h. A blank group was set as the negative control. The antibacterial activity of the hydrogel was evaluated by counting the colony-forming units (CFU). Additionally, 100 µL of Staphylococcus aureus and Escherichia coli suspension (10^7 CFU mL^{-1}) were evenly spread on agar plates, followed by the placement of hydrogel samples with the same volume. After incubation at 37 °C for 18 h, a drug sensitivity disk group was set as the positive control, and the diameter of the inhibition zone was measured for each group. *S. mutans* (ATCC 25175), a common pathogenic bacterium in the oral cavity, often causes dental caries and pulpitis. The acidic metabolic products secreted by this bacterium are detrimental to the healing of oral wounds. In this study, the bactericidal effect of the hydrogel on Streptococcus mutans was investigated using the LIVE/DEAD BacLight Bacterial Viability Kit (Invitrogen L-7012, USA). In short, the hydrogel samples were co-cultured with 1 mL logarithmic phase Streptococcus mutans for 12 hours. As a control group, 1 mL of bacterial suspension was added to 0.2 mL of physiological saline. The bacteria were stained according to the instructions of the kit, and 5 µL of the staining solution was observed under a fluorescence microscope. In the presence of a suitable mixture of SYTO 9 and propidium iodide (PI) staining reagents, bacteria with intact cell membranes were stained green, while bacteria with damaged membranes were stained red. The proportion of live and dead bacteria was evaluated based on the fluorescence intensity.

Wound Healing Effect of Hydrogels in a Mucosal Defect Rat Model: To investigate the effect of PAA-SA@rGO on the healing of oral infected wounds, we established a full-thickness defect model in the buccal mucosa of rats. In brief, 20 male SD rats (8 weeks old, weighing 200–240 g) were divided into 4 groups with $n = 5$ in each group. Anesthesia was induced by intraperitoneal injection of 3 wt% pentobarbital sodium (30 mg k^{-1}g). The surgical area was disinfected, and under sterile conditions, a $5 \times 5 \times 4$ mm^3 wound was created in the buccal mucosa of SD rats using a high-speed turbine and tissue scissors. The wound was then coated with 100 µL of *S. mutans* bacterial solution at a concentration of 10^7 CFU mL^{-1}. Subsequently, hydrogel samples and a commercial dressing (b-FGF gel) were implanted, while no treatment was applied as the blank control group. The wound changes were observed and photographed on days 0, 3, 7, and 10. The wound area was analyzed using Image J software, and the wound healing rate was determined using the following formula:

$$\text{Wound healing rate} = (1 - \text{the } N\text{th day wound area/total wound area}) \times 100\% \quad (3)$$

Histological Analysis: SD rats were euthanized at 12 h, 7 days, and 10 days post-surgery, and mucosal tissue samples around the wounds were collected for histological analysis. In brief, tissue samples collected at 12 h were snap-frozen in liquid nitrogen and cryosectioned to produce frozen sections. Immunofluorescence staining of the antioxidant factors Nrf2 and HO-1 was performed on these sections, followed by observation and photography under a laser confocal microscope. Tissue samples collected at 7 and 14 days were fixed in 10% neutral formalin and embedded in paraffin to produce paraffin sections. H&E and Masson staining were performed on these sections. In addition, we analyzed the expression of early inflammatory factors TNF-α and IL-6, as well as the expression of Col-1 and CD31 involved in tissue repair, using immunohistochemical staining in the wound area. Microscopic observation and photography were conducted, and Image J software was used to analyze the expression of collagen fibers and immune markers to evaluate the wound healing effect.

Effects of Hydrogels on Physiological Potentials: As one of the important ways of intercellular communication, electrophysiological signals are transmitted more frequently when the external environment changes. In

order to verify the effect of different hydrogel systems on the electric field at the wound site, we constructed an extracellular electrical signal pathway to detect the resistance and voltage–time changes at the wound site. In brief, we first anesthetized and fixed SD rats, and then prepared a wound model on the buccal mucosa of the rats. After implanting different dressings on the wound, a multimeter was used to measure the resistance at both ends of the wound, and a self-built electrical signal monitoring device was used to record the potential difference between the deep part of the wound and the wound edge. All electrical signals were plotted using the Keithley 2400 SourceMeter and a box temperature control.

Statistical Analysis: Statistical analysis was conducted by using GraphPad Prism 8 statistical software. Significant differences were calculated with Student's *t* test or by one-way analysis of variance (ANOVA), followed by the Tukey's multiple comparison tests when performing multiple comparisons between groups. Data represent the Mean ± SD of at least three replicates. $*P < 0.05$, $**P < 0.01$ and $***P < 0.001$, were regarded as statistically significant. In addition, "ns" denoted no significant difference.

Supporting Information

Supporting Information is available from the Wiley Online Library or from the author.

Acknowledgements

This work was sponsored by the National Natural Science Foundation of China (82100993, 62305068, 62075100, 62074044, 61904036, and 61675049), Project of Shanghai Stomatological Hospital (SHH-2022-YJ-07, SSH-2022-KJCX-B06), Shanghai Municipal Health commission Planning (202140503), China Postdoctoral Science Foundation (2022M720747), Shanghai Post-doctoral Excellence Program (2021016), Shanghai Rising-Star program (22YF1402000), Zhongshan-Fudan Joint Innovation Center and Jihua Laboratory Projects of Guangdong Province (X190111UZ190), is gratefully acknowledged.

Conflict of Interest

The authors declare no conflict of interest.

Author Contributions

Q.Z., H.D., and K.Y. contributed equally to this work. H.D., Q.Z., and K.Y. conceived and designed the project. W.Z., M.Z., Z.Q., and R.G. put forward many constructive suggestions and helped the implementation of the project. Q.Z., K.Y., and H.D. performed all data collection. Q.Z. and H.D. conducted the analysis of experimental data. H.D. conducted the theoretical calculations. H.D. and Q.Z. wrote the manuscript. Q.Z., H.D., X.W., and R.G. corrected the manuscript. Others carried out auxiliary work related to these experiments.

Data Availability Statement

The data that support the findings of this study are available from the corresponding author upon reasonable request.

Keywords

conductive hydrogel, microphysiological electric field, oral mucosal disease, tissue regeneration

Received: September 18, 2023
Revised: January 9, 2024
Published online:

[1] A. I. Toma, J. M. Fuller, N. J. Willett, S. L. Goudy, *Transl. Res.* **2021**, *236*, 17.
[2] W. G. Wade, *Periodontology 2000* **2021**, *86*, 113.
[3] F. Chen, X. Liu, X. Ge, Y. Wang, Z. Zhao, X. Zhang, G.-Q. Chen, Y. Sun, *Chem. Eng. J.* **2023**, *451*, 138899.
[4] W. Qi, N. Dong, L. Wu, X. Zhang, H. Li, H. Wu, N. Ward, J. Yu, H. Liu, J. Wang, X. Deng, R. C. Zhao, *Bioact. Mater.* **2023**, *23*, 53.
[5] W. Zhang, B. Bao, F. Jiang, Y. Zhang, R. Zhou, Y. Lu, S. Lin, Q. Lin, X. Jiang, L. Zhu, *Adv. Mater.* **2021**, *33*, 2105667.
[6] R. Dong, B. Guo, *Nano Today* **2021**, *41*, 101290.
[7] K. Schenck, O. Schreurs, K. Hayashi, K. Helgeland, *Int. J. Mol. Sci.* **2017**, *18*, 386.
[8] J. C. J. Holzer-Geissler, S. Schwingenschuh, M. Zacharias, J. Einsiedler, S. Kainz, P. Reisenegger, C. Holecek, E. Hofmann, B. Wolff-Winiski, H. Fahrngruber, T. Birngruber, L.-P. Kamolz, P. Kotzbeck, *Biomedicines* **2022**, *10*, 856.
[9] F. Zarei, M. Soleimaninejad, *Artif. Cells, Nanomed., Biotechnol.* **2018**, *46*, 906.
[10] J. Chen, Y. Liu, G. Cheng, J. Guo, S. Du, J. Qiu, C. Wang, C. Li, X. Yang, T. Chen, Z. Chen, *Small* **2022**, *18*, 2201300.
[11] C. Tu, H. Lu, T. Zhou, W. Zhang, L. Deng, W. Cao, Z. Yang, Z. Wang, X. Wu, J. Ding, F. Xu, C. Gao, *Biomaterials* **2022**, *286*, 121597.
[12] Z. Xu, B. Liang, J. Tian, J. Wu, *Biomater. Sci.* **2021**, *9*, 4388.
[13] F. Xu, Q. Zhang, S. Liu, Y. Zhao, *Mater. Today Commun.* **2023**, *35*, 105634.
[14] M. Zhao, M. Rolandi, R. R. Isseroff, *Cold Spring Harbor Perspect. Biol.* **2022**, *14*, a041236.
[15] M. Zhao, *Electrical Fields in Wound Healing—An Overriding Signal that Directs Cell Migration[C]//Seminars in Cell & Developmental Biology*, Academic, Sand Diego, CA **2009**, Vol. *20*, pp. 674–682.
[16] S. Abounit, C. Zurzolo, *J. Cell Sci.* **2012**, *125*, 1089.
[17] M. Levin, *BioEssays* **2012**, *34*, 205.
[18] M. Levin, *Mol. Biol. Cell* **2014**, *25*, 3835.
[19] J. Mathews, M. Levin, *Curr. Opin. Biotechnol.* **2018**, *52*, 134.
[20] C. D. McCaig, A. M. Rajnicek, B. Song, M. Zhao, *Physiol. Rev.* **2005**, *85*, 943.
[21] L. Cao, J. Pu, M. Zhao, *Cell. Mol. Life Sci.* **2011**, *68*, 3081.
[22] R. Balint, N. J. Cassidy, S. H. Cartmell, *Tissue Eng., Part B* **2013**, *19*, 48.
[23] S. Meng, M. Rouabhia, Z. Zhang, *Materials* **2021**, *15*, 165.
[24] R. Luo, J. Dai, J. Zhang, Z. Li, *Adv. Healthcare Mater.* **2021**, *10*, 2100557.
[25] C. Chen, X. Bai, Y. Ding, I.-S. Lee, *Biomater. Res.* **2019**, *23*, 1.
[26] Y. J. Cheah, M. R. Buyong, M. H. Mohd Yunus, *Polymers* **2021**, *13*, 3790.
[27] J. Tian, R. Shi, Z. Liu, H. Ouyang, M. Yu, C. Zhao, Y. Zou, D. Jiang, J. Zhang, Z. Li, *Nano Energy* **2019**, *59*, 705.
[28] J. Wang, J. Lin, L. Chen, L. Deng, W. Cui, *Adv. Mater.* **2022**, *34*, 2108325.
[29] P. Liu, K. Jin, W. Wong, Y. Wang, T. Liang, M. He, H. Li, C. Lu, X. Tang, Y. Zong, C. Li, *Chem. Eng. J.* **2021**, *415*, 129025.
[30] S.-H. Jeong, Y. Lee, M.-G. Lee, W. J. Song, J.-U. Park, J.-Y. Sun, *Nano Energy* **2021**, *79*, 105463.
[31] X.-F. Wang, M.-L. Li, Q.-Q. Fang, W.-Y. Zhao, D. Lou, Y.-Y. Hu, J. Chen, X.-Z. Wang, W.-Q. Tan, *Bioact. Mater.* **2021**, *6*, 230.
[32] G. Conta, A. Libanori, T. Tat, G. Chen, J. Chen, *Adv. Mater.* **2021**, *33*, 2007502.
[33] X. Kong, J. Fu, K. Shao, L. Wang, X. Lan, J. Shi, *Acta Biomater.* **2019**, *100*, 255.
[34] A. M. Overmiller, A. P. Sawaya, E. D. Hope, M. I. Morasso, *Cold Spring Harbor Perspect. Biol.* **2022**, *14*, a041244.
[35] C. L. Ferreira, M. A. Neves Jardini, C. M. Moretto Nunes, D. V. Bernardo, R. C. Viana Casarin, E. dos Santos Gedraite, M. A. Mathias,

F. Liu, G. Mendonça, D. B. Silveira Mendonça, M. P. Santamaria, *Arch. Oral Biol.* **2021**, *122*, 105028.
[36] F. Strietzel, R. Martín-Granizo, S. Fedele, L. Lo Russo, M. Mignogna, P. Reichart, A. Wolff, *Oral Dis.* **2007**, *13*, 206.
[37] B. Kim, J. Park, J. Y. Lee, *Korean J. Chem. Eng.* **2023**, *40*, 352.
[38] P. Tang, L. Han, P. Li, Z. Jia, K. Wang, H. Zhang, H. Tan, T. Guo, X. Lu, *ACS Appl. Mater. Interfaces* **2019**, *11*.
[39] S. A. Laura, V. Ruiz, P. S. Adrián, H. Grande, I. Loinaz, D. Dupin, *J. Mater. Sci.* **2021**, *56*, 10041.
[40] G. Wang, F. Yang, W. Zhou, N. Xiao, M. Luo, Z. Tang, *Biomed. Pharmacother.* **2023**, *157*, 114004.
[41] S. Hussain, S. Maktedar, Structural Results Chem **2023**, *6*, 101029.
[42] Y. Zhang, Z. Wang, Q. Sun, Q. Li, S. Li, X. Li, *Materials* **2023**, *16*, 5161.
[43] Q. Li, B. Tian, J. Liang, W. Wu, *Mater. Chem. Front.* **2023**, *7*, 2925.
[44] A. Kumar, K. M. Rao, S. S. Han, *Chem. Eng. J.* **2017**, *317*, 119.
[45] J. Yi, K. T. Nguyen, W. Wang, W. Yang, M. Pan, E. Lou, P. W. Major, L. H. Le, H. Zeng, *J. Colloid Interface Sci.* **2020**, *578*, 598.
[46] J. Qiu, D. Wang, H. Geng, J. Guo, S. Qian, X. Liu, *Adv. Mater. Interfaces* **2017**, *4*, 1700228.
[47] J. Sun, T. Chen, B. Zhao, W. Fan, Y. Shen, H. Wei, M. Zhang, W. Zheng, J. Peng, J. Wang, Y. Wang, L. Fan, Y. Chu, L. Chen, C. Yang, *ACS Appl. Mater. Interfaces* **2022**, *15*, 416.
[48] J. Zhu, Y. Li, W. Xie, L. Yang, R. Li, Y. Wang, Q. Wan, X. Pei, J. Chen, J. Wang, *ACS Appl. Mater. Interfaces* **2022**, *14*, 53575.
[49] Q. Zhang, C. Qian, W. Xiao, H. Zhu, J. Guo, Z. Ge, W. Cui, *RSC Adv.* **2019**, *9*, 18344.
[50] J. H. Lee, K. E. Lee, O. H. Nam, Y. K. Chae, M.-H. Lee, D.-K. Kweon, M. S. Kim, H.-S. Lee, S. C. Choi, *J. Dent. Sci.* **2022**, *17*, 1595.
[51] N. Nagai, R. Seiriki, S. Deguchi, H. Otake, N. Hiramatsu, H. Sasaki, N. Yamamoto, *Pharmaceutics* **2020**, *12*, 532.
[52] Y. Yang, J. Yuan, Y. Ni, Y. Gu, J. Zhou, W. Yuan, S. Xu, L. Che, S. Y. Zheng, W. Sun, D. Zhang, J. Yang, *Composites, Part B* **2022**, *243*, 110119.
[53] R. Iglesias-Bartolome, A. Uchiyama, A. A. Molinolo, L. Abusleme, S. R. Brooks, J. L. Callejas-Valera, D. Edwards, C. Doci, M.-L. Asselin-Labat, M. W. Onaitis, N. M. Moutsopoulos, J. Silvio Gutkind, M. I. Morasso, *Sci. Transl. Med.* **2018**, *10*, eaap8798.
[54] S. Polaka, P. Katare, B. Pawar, N. Vasdev, T. Gupta, K. Rajpoot, P. Sengupta, R. K. Tekade, *ACS Omega* **2022**, *7*, 30657.
[55] Y. Xiong, X. Chu, T. Yu, S. Knoedler, A. Schroeter, L. Lu, K. Zha, Z. Lin, D. Jiang, Y. Rinkevich, A. C. Panayi, B. Mi, G. Liu, Y. Zhao, *Adv. Healthcare Mater.* **2023**: 2300779.